

Energy- and angle-resolved spectral phases via semirelativistic *ab initio* RABBITT simulationsLuke Roantree ^{*}, Jack Wragg, Hugo van der Hart, and Andrew Brown [†]*Centre for Light Matter Interaction, School of Mathematics and Physics, Queen's University Belfast, Belfast BT71NN, United Kingdom*

(Received 25 January 2023; revised 28 June 2023; accepted 18 July 2023; published 8 August 2023)

We simulate the so-called “rainbow reconstruction of attosecond beating by interference of two-photon transitions” (Rainbow RABBITT) technique with R-matrix with time-dependence (RMT) theory for neutral argon. We compute the energy-resolved spectral phase induced by the autoionizing $[\text{Ne}]3s3p^64p\ ^1P$ resonance with simulations incorporating semirelativistic atomic descriptions. This allows us to isolate the $j = 1/2$ and $j = 3/2$ spin-orbit component contributions to the energy-resolved spectral phase and compare these against experiment. We analyze changes to the spectral phase resolved in energy and emission angle induced by the autoionizing state.

DOI: [10.1103/PhysRevA.108.023112](https://doi.org/10.1103/PhysRevA.108.023112)**I. INTRODUCTION**

Attoscience provides several tools for investigating ultrafast processes with high temporal precision [1,2]. One such tool which allows the investigation of electron ionization paths and the interference between them, is the “reconstruction of attosecond beating by interference of two-photon transitions” (RABBITT) method [3,4]. In RABBITT, the photoelectron spectrum arising from two-photon absorption in a combined infrared (IR) and extreme ultraviolet (XUV) field is measured as a function of the time delay between the IR and XUV. Interference between competing ionization pathways creates oscillations in the photoelectron yield [5–7]. The phase of these oscillations can then be attributed to the phase differences in the harmonic components of the XUV pulse and the intrinsic phase differences of the ionization pathways [8,9].

Figure 1 elucidates the key ideas of the basic RABBITT technique via an energy-level description. Initially, a driving IR laser is used to initiate a high-harmonic generation process, creating an “attosecond pulse train” (APT) of XUV energy components, with each component an odd harmonic of the driving IR frequency [3,5]. The combined IR and APT then dress the gas target under investigation, where (a) an XUV photon promotes a valence electron from the ground state to the continuum and then (b) the absorption or emission of an IR photon leads to the formation of a “sideband” which can be reached by two competing pathways; a sideband with an energy above the ground state of $2n$ times the IR energy may be reached by absorption of a $(2n - 1)$ -th harmonic XUV photon and absorption of an IR photon, or by absorption of

a $(2n + 1)$ -th harmonic XUV photon and emission of an IR photon [6,7]. The interference between these two ionization paths is encoded in the measured photoelectron energy spectrum, which varies in a “beating pattern” as a function of XUV-IR time delay [5,10]. Analyzing this beating pattern then unveils the phase information about the interfering pathways, and variation in this phase between or within sidebands can be related to variation in ionization delays experienced by the electron in the two paths and informs our understanding of the underlying atomic- or measurement-induced processes [9,11]. The “Rainbow RABBITT” technique extends RABBITT by resolving the spectra in energy, enabling investigation of the change in interference with energy [7,12]. This is of particular interest for probing autoionizing resonances, where the outgoing wave functions are marked by a rapid change in phase with energy [12].

With sufficient resolution in energy, it has recently been demonstrated that it is also possible to distinguish ionization pathways involving fine-structure splittings [13]. In 2016, Kotur *et al.* measured the spectral phase across the $3s3p^64p$ ($3s^{-1}4p$) window resonance in argon through application of the Rainbow RABBITT technique and interpreted the variation in spectral phase via the interference between the continuum $3p \rightarrow \epsilon s/\epsilon d$ states and the quasi-bound $3s^{-1}4p$ state. In 2020, Turconi *et al.* extended this work by resolving the spectral phase across the same $3s^{-1}4p$ resonance for both the $j = 1/2$ and $j = 3/2$ spin-orbit (SO) components of the residual Ar^+ ion [13]. The features obtained were nearly overlapping due to the small (0.177 eV) SO splitting of the $^2P^o$ threshold. The individual SO component contributions were resolved under the assumption they were identical, except that they differed in energy by the SO splitting of the $^2P^o$ threshold and in magnitude by the $j = 1/2$ and $j = 3/2$ threshold degeneracies [14].

For heavier atomic systems, or molecules, the SO splitting may be significantly larger, and we speculate that the assumption that the individual SO components can be treated as scaled-and-shifted copies may not be valid in such cases. Moreover, the dynamics associated with these larger energy gaps may evolve on timescales comparable to the laser pulse

^{*}lroantree01@qub.ac.uk[†]andrew.brown@qub.ac.uk

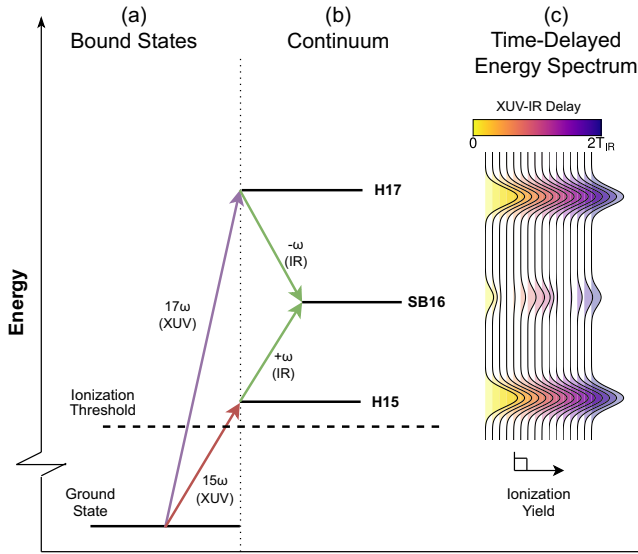


FIG. 1. Energy-level diagram describing available ionization paths during a generalized RABBITT experiment. Region (a) shows the relative positions of the ground state and ionization threshold relative to the XUV photon energies, while region (b) shows notable energies in the photoelectron energy spectrum which can be reached via one-photon processes (H15 and H17) or two-photon processes (SB16). Region (c) shows example photoelectron energy spectra for a range of XUV-IR delays to demonstrate the “beating” inherent to the interference pattern of SB16 from which the spectral phase may be extracted.

duration [15]. For these reasons, here we demonstrate a more general approach to this problem that does not rely on these same modeling assumptions.

In this paper we use R-matrix with time-dependence (RMT) calculations with a SO-corrected *ab initio* argon description to disentangle the SO components of the phase across the $3s^{-1}4p$ resonance directly [16,17]. We also extend the previous work by investigating the dependence of spectral phase on emission angle [18–21]. Most recent investigations using extensions of the RABBITT technique generally resolve the spectral phase in either emission angle or energy [13,19,22]. To our knowledge only one other published study demonstrates RABBITT spectra resolved in both emission angle and energy [21]. We further analyze the spectral phase resolved in energy and angle (SPREA) in terms of the contributions of ionization pathways involving different SO components.

II. METHODOLOGY

A. RABBITT investigation overview

Figure 2 displays the specific ionization pathways relevant for the present work, including pathways via the autoionizing $3s3p^64p$ ($3s^{-1}4p$) state. The XUV attosecond pulse train is constructed using a “comb” of the odd harmonics of the IR. The driving IR frequency is selected such that the 17th harmonic (H17) will probe the $3s^{-1}4p$ autoionizing state in Ar, which decays to leave Ar^+ in either the $^2P_{3/2}^o$ or $^2P_{1/2}^o$ final state. H17 photons can either ionize an electron directly, or excite it to the autoionizing $3s^{-1}4p$ state. In either case,

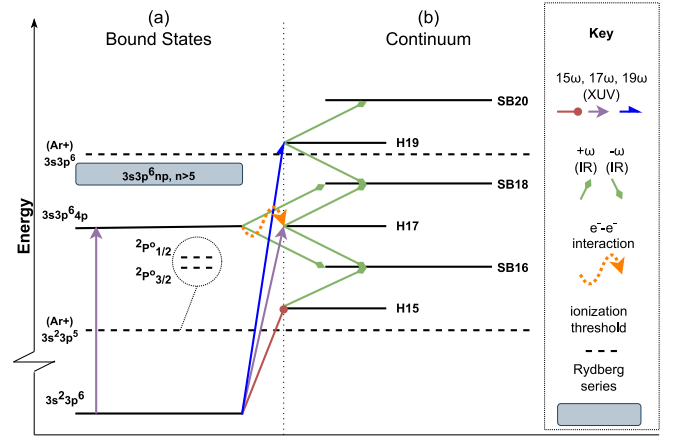


FIG. 2. Energy-level diagram describing available ionization pathways during a RABBITT experiment targeting the $3s3p^64p$ autoionizing state in argon. The direct pathway involves (a) promoting an electron from the ground state to the continuum via absorption of an XUV photon (H15, H17, or H19). The indirect pathway involves (a) promoting an electron from the $3s$ shell to the autoionizing $[\text{Ne}]3s3p^64p$ state, which coincides in energy with H17. In either case subsequent absorption or emission of an IR photon (b) results in photoelectrons in sidebands (SB) 16, 18, or 20. The direct and indirect pathways to H17 interfere, “imprinting” the resonance in the neighboring sidebands (SB16 and SB18). The ionization threshold is split by the spin-orbit (SO) interaction. The photoelectrons can be coupled with either of the two thresholds, resulting in a “splitting” of the harmonics and sidebands, with each part corresponding to one of the two SO-split residual ion states.

subsequent absorption or emission of an IR photon will leave the photoelectron with an energy corresponding to sideband 18/16 (SB18/16). These direct and indirect pathways to SB18/16 produce an interference pattern which affords the extraction of imparted resonance information via extraction of spectral phase, described in Sec. II E [5,10].

B. R matrix with time dependence

To carry out the simulated RABBITT investigation, we require a detailed description of the neutral argon system. The R-matrix approach provides an accurate and computationally efficient description of an atomic system by dividing space into two distinct regions: an “inner” region sufficiently large to contain the final states of the residual ion, and an “outer” region in which a single electron moves in the long-range field of the residual ion. Within the inner region, multielectron interactions are included, while in the outer region, the photoelectron is spatially isolated from the residual electrons and electron exchange is neglected [23].

RMT extends this concept into the time domain, allowing the description of atomic and molecular systems driven by short laser pulses. It takes an initial R-matrix description of the system and propagates the wave function through time by solving the time-dependent Schrödinger equation, including a time-dependent potential for the laser field [16].

To describe relativistic effects, however, we require solutions of the Dirac equation, solutions to which can be well approximated for light atomic systems by solving the

Schrödinger equation with a Breit-Pauli Hamiltonian [24]. This Breit-Pauli Hamiltonian can be considered as a first-order perturbative correction to the nonrelativistic description and adds three independent terms which describe physical effects: the Darwin term, mass correction term, and SO interaction term. Within this semirelativistic approximation, the jK coupling, also called “intermediate coupling,” is used in contrast with the original LS -coupling scheme. In this coupling scheme, the total angular momentum J is given by $K + s_e$, with s_e the spin of the outer electron and K given by $J_{ri} + l_e$, where J_{ri} is the total angular momentum of the residual ion state and l_e is the orbital angular momentum of the outer electron.

So far the developments made to the RMT code enable the inclusion of only the SO interaction term, under the additional approximation that electron screening of the nuclear potential can be neglected. This capability has been demonstrated in an investigation of dynamics mediated by the SO interaction [17]. The Darwin and mass-correction terms are smaller corrections to the nonrelativistic dynamics and can each be optionally included [24].

C. Atomic structure

The atomic structure description uses the R-matrix basis previously developed for single-photon ionization of Ar [25]. The basis comprises $1s$, $2s$, $2p$, $3s$, and $3p$ Hartree Fock orbitals for the residual ion (Ar^+) ground state, and additional $4s$, $4p$, and $3d$ pseudo-orbitals. This combination has been shown to give a good description of single- and multiphoton ionization of Ar [25,26]. An R-matrix boundary of 20 a.u. was found to be sufficiently large to contain the residual ion [23].

We include the $[\text{Ne}]3s^23p^5^2P_{1/2}^o$, $[\text{Ne}]3s^23p^5^2P_{3/2}^o$, and $[\text{Ne}]3s3p^6^2S^e$ states of Ar^+ , allowing ionization into all $[\text{Ne}]3s^23p^5 \epsilon l(K)s$ and $[\text{Ne}]3s3p^6 \epsilon l(K)s$ channels up to a maximum total angular momentum of $J_{\text{max}} = 6$. This value of J_{max} is sufficiently high to give converged results, and increasing the value of J_{max} beyond this becomes prohibitively expensive.

Using the atomic description described previously, the gap between the two SO split thresholds for a purely *ab initio* calculation is found to be 154 meV and the $^2S_0^e$ threshold to lie 13.62 eV above the $^2P_{3/2}^o$ threshold. We then manually apply small shifts the two $^2P_j^o$ ionization thresholds such that they align with the 15.76-eV ($^2P_{3/2}^o$) and 15.94-eV ($^2P_{1/2}^o$) NIST-recorded values [27], with a 177-meV SO splitting. Similarly, we shift the $^2S_0^e$ threshold to the reference value (29.24 eV). Together, these shifts result in a small difference from the purely *ab initio* calculation but ensure a good overall description is maintained for states below the $^2S_0^e$ threshold and that the SO splitting matches the NIST value, resulting in an accurate description of dynamical SO interaction effects throughout the simulation. The energy level of the state of interest, the $[\text{Ne}]3s3p^64p$, achieves excellent agreement with NIST with this description, at 26.59 eV above the ground state.

D. Simulation design

We use the RMT code suite to simulate a full RABBITT experiment of the atomic system described in Sec. II C [16].

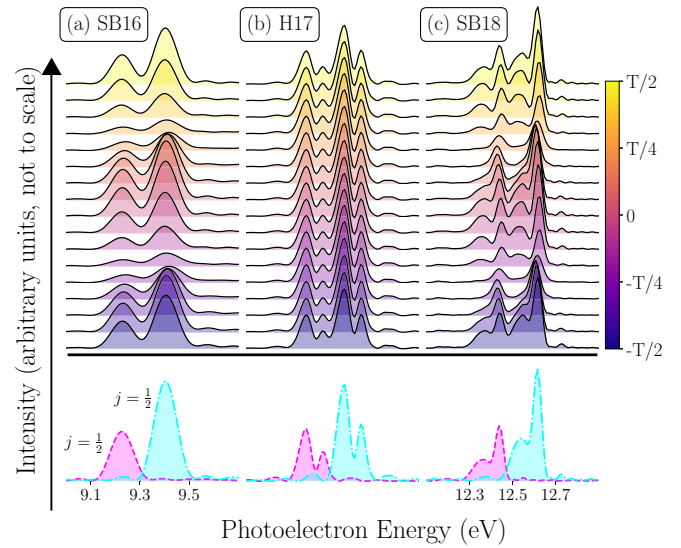


FIG. 3. Photoelectron spectra for the resonant harmonic H17 (b) and its neighboring sidebands (a) SB16 and (c) SB18 for each of the APT-IR delays used in RABBITT simulations (top) and the spectra corresponding to a single APT-IR delay (bottom) decomposed into the individual $j = 1/2$ (magenta, dashed) and $j = 3/2$ (cyan, dot-dashed) SO contributions. The oscillations in the sideband yields as a function of APT-IR delay are characteristic of the interference between the two ionization pathways: H15 plus an IR photon and H17 minus an IR photon for SB16, and H17 plus an IR photon and H19 minus and IR photon for SB18. These spectra were generated from a driving IR wavelength of 788.0 nm.

Simulations are carried out for a range of driving IR wavelengths between 785 and 789 nm. These wavelength ranges are selected to scan the 17th harmonic across the $3s^{-1}4p$ resonance to provide a complete description of the imparted phase.

For each of these IR wavelengths, electric fields are designed for RABBITT “snapshots,” corresponding to a specific delays between the IR and XUV (IR field remains constant between snapshots, with the XUV field delayed). For each wavelength we simulate 16 snapshots with delays ranging between ~ -1.26 and 1.26 fs (spanning $-T_{\text{IR}}/2$ to $T_{\text{IR}}/2$, where T_{IR} is the period of oscillation for an IR wavelength).

The total electric field is constructed by adding IR and XUV component fields. The IR field has a peak intensity of 2.5×10^{10} W/cm² and comprises 16 cycles, of which the first and last two have a \sin^2 turn-on/turn-off. The XUV APT comprises 16, five-cycle XUV pulses and spans harmonics 13 to 21 of the driving IR, with its peak at the 17th harmonic at an intensity of 5×10^9 W/cm². We continue the simulation beyond the end of the electric fields for an additional 55 fs.

We note that at variance with standard analyses of experimental RABBITT spectra, we do not need to eliminate the phase contribution of the APT by subtracting a reference sideband as we construct our APT without chirp.

E. Phase extraction

Figure 3 shows the photoelectron yield as a function of energy in the regions of the seventeenth harmonic (H17)

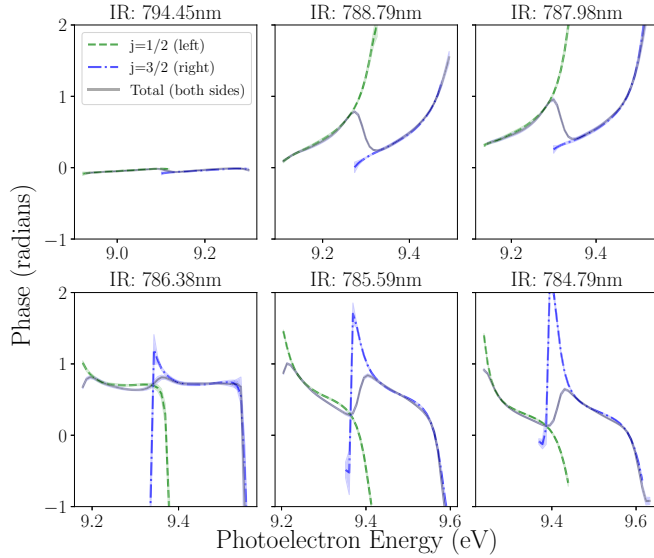


FIG. 4. Spectral phases extracted across SB16 for six driving IR wavelengths “scanning” across the $3s^{-1}4p$ resonance at H17. In each figure the total extracted phase is shown with the black solid curve, and the phases for the individual Ar^+ , $3s^23p^5$ thresholds are shown with the (left, $j = 1/2$) green dashed and (right, $j = 3/2$) blue dot-dashed curves. For comparison, the 794.45-nm result (top left) shows the expected flat phase off-resonance.

and the neighboring sidebands (SB16 and SB18) for an IR wavelength of 788 nm. Each peak contains two distinct contributions, one from each of the $j = 1/2$ and $j = 3/2$ components. This is verified by plotting each component in isolation in the lower panel ($j = 1/2$ in magenta dashed and $j = 3/2$ in cyan dot-dashed). We note the resonance imprints, visible in the H17 region of the spectrum, cannot be directly observed in SB16. Instead, the effects of the resonance imprints within SB16 become apparent upon the extraction of the spectral phase, which we now describe.

We calculate the photoelectron energy distribution for a range of XUV-IR time delays (shown in top section of Fig. 3). These show the typical interference pattern for a RABBITT process: a sinusoidal oscillation with a period of $T_{\text{IR}}/2$. A trust region reflective algorithm was used to fit curves of the form [3,4,6]

$$f(t, a^*, \phi^*, b^*) = a^* \cos(2\omega_{\text{IR}}t + \phi^*) + b^*$$

to the sideband yields at each energy point, where t is the XUV-IR time delay and ‘*’ indicates a fitted parameter [28]. The fitted parameter ϕ^* is the spectral phase from the competing ionization paths, and we use the calculated standard deviation of ϕ^* as an estimate for the error associated with the fitting procedure.

III. RESULTS

A. Rainbow-RABBITT scans

Figure 4 shows the spectral phases across SB16 for a range of driving IR wavelengths. Changes to the spectral phase across the sideband originate from the resonance imprint. Off-resonance, a relatively flat phase of approximately 0 is

observed for 794.5 nm (top left panel). This is expected as the background phase is nearly constant, and the harmonic components of the APT are in phase. The phase changes observed, then, can be attributed primarily to the $3s^{-1}4p$ resonance. For each wavelength we observe two phase jumps corresponding to the $[\text{Ne}]3s^23p^5 \ ^2P_{3/2}^o$ & $\ ^2P_{1/2}^o$ final states of the Ar^+ ion.

RMT permits the direct resolution of the $j = 1/2$ and $j = 3/2$ electron emission channels, from which we can extract the individual contributions to the overall spectral phase. Figure 4 also shows these individually computed $j = 1/2$ and $j = 3/2$ contributions for each wavelength. The $j = 1/2$ contributions are similar to their corresponding $j = 3/2$ contributions but spectrally shifted by 177 meV, matching the SO splitting of the Ar^+ ionization threshold.

Figure 4 shows significant changes to the extracted phase as a function of wavelength. For the relatively weak fields in this simulation, the physics of the underlying resonance will not significantly be affected by these variations in IR wavelength. Hence the changes to the resonance imprint relate primarily to the coupling between the resonance and the ground state. As the IR wavelength decreases, the energy of the associated 17th harmonic increases, and the energy of the ground state plus a H17 photon moves from below the $3s^{-1}4p$ resonance to above it. This results in significant changes to the profiles of the imprinted resonances in SB16 as a function of photoelectron energy. At a wavelength of 786.38 nm, we note that the resonance leads to a relatively flat, nonzero phase across the entire sideband.

B. Comparison with previous work

Previous work has demonstrated a method of resolving SO contributions in the RABBITT spectra. This amounts to a *post hoc* analysis based on the assumption that the individual SO contributions are identical, except for a shift in energy (by the SO splitting of the $\ ^2P^o$ threshold) and a scaling in magnitude (by the $j = 1/2$ and $j = 3/2$ threshold degeneracies) [13,14]. A full description, and derivation, of the *post hoc* analysis method is given in Supplementary Note 4 of Ref. [14].

In our direct calculations, by contrast, the splitting is built into the atomic structure, and thus by selecting the corresponding electron emission channels one can extract the phase associated with an individual SO threshold. Additionally, in principle the simulations include any SO dynamics that may evolve [15] which would not be captured by a *post hoc* analysis of a nonrelativistic calculation, although we note that in the current case no such dynamics are apparent.

To facilitate comparison with experimental data, we use RMT results for one driving wavelength (788 nm) selected to give the best qualitative agreement with the experimentally obtained delay-averaged spectrum for H17. Figure 5 shows the total and SO-resolved spectral phase across sidebands 16, 18, and 20 from experiment [13] and RMT. For SB16 [Fig. 5(a)] there is good agreement for the total and SO-resolved spectral phase. Although the double structure is evident in SB18, the agreement with experiment is not as good as for SB16. This we attribute to limitations in the atomic structure description: SB18 can excite autoionizing resonances with $J = 0$ or $J = 2$, which are not optimally

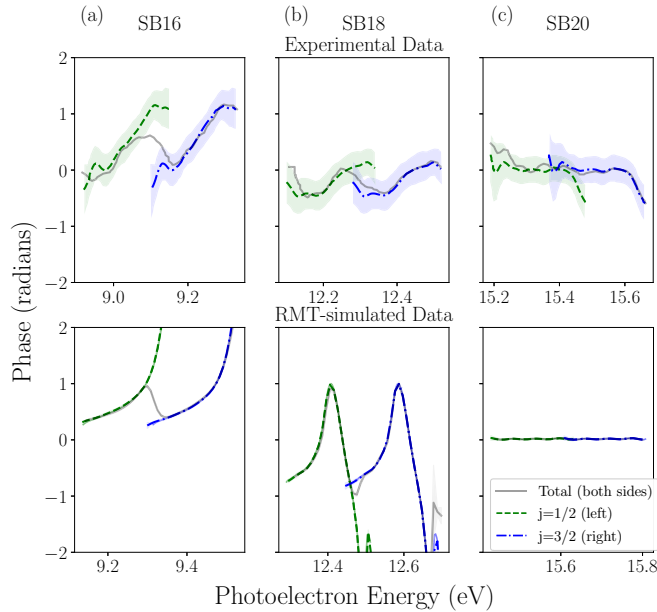


FIG. 5. Spectral phases extracted across (a) SB16, (b) SB18, and (c) SB20, from experiment (top) [13] and RMT simulations (bottom). For each we present the total (black, solid) and threshold-resolved ($j = 1/2$, green, dashed, left and $j = 3/2$, blue, dot-dashed, right) spectral phases. The experimental data is threshold resolved using a *post hoc* analysis procedure described in Refs. [13,14], while the simulation data is threshold resolved through direct isolation of threshold contributions to the photoelectron wave function. The IR wavelength in experiment was 791 nm, whereas in the RMT simulations a wavelength of 788 nm resulted in the best qualitative agreement with the experimentally obtained delay-averaged spectrum for H17.

positioned compared to the $3s^{-1}4p$ resonance on which we focus, and so it is not unexpected that the resulting spectrum differs from experiment in this region. The spectral phase across both components of SB20 appears flat, indicating no resonance imprint, in line with the experimental results.

C. Angle-resolved spectral phases

Recent RABBITT studies have started to investigate the spectral phase as a function of electron emission angle [19,21,29,30]. The experimentally obtained photoelectron angular distribution (PAD) can shed light on the partial wave composition of the photoelectron wave function. Fitting the PAD with a combination of spherical harmonics reveals the amplitude and phase of the individual partial waves involved [19]. In our simulations we instead have direct access to the partial wave composition of the photoelectron wave function. Modern experiments have generally demonstrated either energy resolution for angle-integrated spectra [13] or angular resolution for energy-integrated sideband spectra [19,22], but our results permit simultaneous evaluation of the SPREA. (We note that one recent study has reported experimental results resolved in both energy and emission angle for helium [21].)

Figure 6 shows the SPREA extracted from the two-dimensional momentum distribution of SB16 for five selected energies, showing the angular behavior of phase at the center

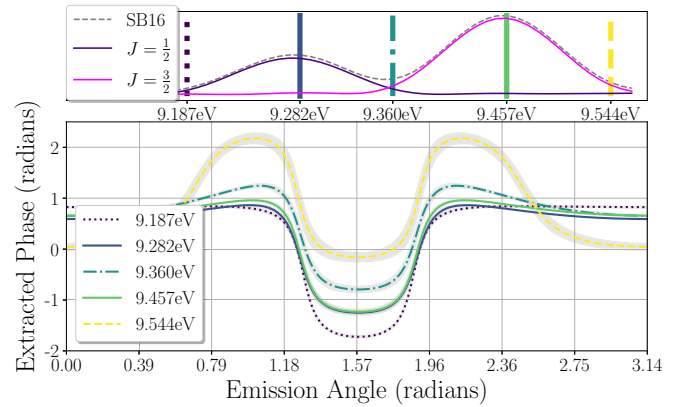


FIG. 6. Emission-angle resolved distributions of spectral phase at representative energies within SB16 for a simulated RABBITT experiment in argon with a 786-nm driving laser wavelength. The upper panel indicates the position of the selected energies within the sideband (vertical bars, with color and brightness varying with increasing energy from purple or dark at the lower sideband limit to yellow or light at the upper limit), while the lower section shows how the angular dependence of the phase behaves at energies at the edges and in the center of the two SO components. The extracted phase for energies 9.282 eV (dark-blue solid) and 9.457 eV (light-green solid) are markedly similar, as these energies are both located in the centers of the SO component sidebands.

and edges of the sideband peaks. In the absence of any resonance, we would expect the SPREA to remain almost constant across a sideband. This is observed for SB14 (not shown, but viewable in Ref. [31]). By contrast, we observe variations in the SPREA between energies across SB16, arising from the $3s^{-1}4p$ resonance.

In spite of the nontrivial variation in the SPREA, we note that at two energies plotted in Fig. 6 (9.282 and 9.457 eV, solid dark-blue and light-green, respectively) an almost identical behavior is observed. These energies are close to the centers of the $j = 1/2$ and $j = 3/2$ peaks. These two peaks are manifestations of the same resonance, with electron emission split between two Ar^+ thresholds. Thus we might expect the $j = 1/2$ and $j = 3/2$ components to produce similar SPREAs, albeit shifted by the SO splitting of 177 meV. This is borne out when treating each of the SO components separately, as we now clarify by viewing the SPREA from a different vantage.

Figure 7 elucidates the correspondence between the $j = 1/2$ and $j = 3/2$ components at selected emission angles by showing the spectral phase as a function of photoelectron energy for a few, selected emission angles. Figure 7(c) shows the SPREA for each SO component separately. The phase at energies below, at, and above the peak match almost exactly between the $j = 1/2$ and $j = 3/2$ components. However, in the total spectrum, shown in Fig. 7(b), the SPREA at energies separated by 177 meV are not identical in general, due to the combined contribution of the two components at intermediate energies where these components overlap. Outside this intermediate energy region, we observe almost identical SPREA behavior between the separate $j = 1/2$ and $j = 3/2$ components at all selected emission angles, for energies separated by 177 meV as expected.

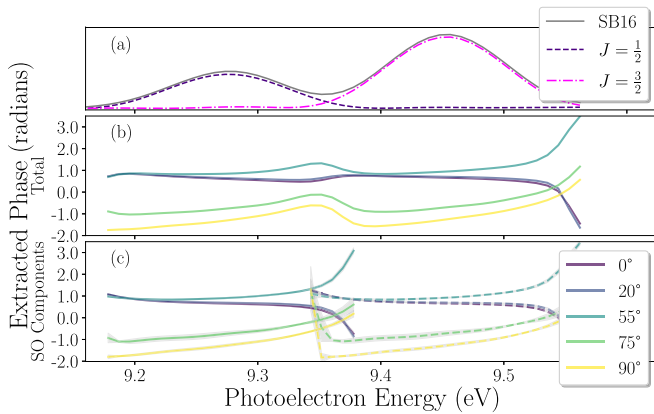


FIG. 7. Energy-resolved distributions of spectral phase evaluated at representative emission angles for a simulated RABBITT experiment in argon with a 786-nm driving laser wavelength: a different perspective on the same data presented in Fig. 6. (a) The ionization yield within SB16, on the same energy axis as the spectral phase presented in (b) and (c). Total (b) and SO (c) component spectral phase, evaluated at five emission angles in each case. The color or brightness of the lines varies with increasing emission angle from purple or dark at 0° to yellow or light at 90° . In (c), the $j = 1/2$ component phases are shown in solid curves, while the $j = 3/2$ component phases are shown in dashed curves, and we observe strong similarity in the behavior of the spectral phase between SO components at the same emission angle.

IV. CONCLUSIONS

We applied the RMT suite of codes to study the influence of the $3s^{-1}4p$ autoionizing state in Ar on RABBITT-style, ejected electron spectra. More detail on the behavior of the spectral phase was obtained by resolving the spectra in both energy and emission angle [16]. Using the Breit-Pauli formalism allowed the inclusion of spin-orbit (SO) interaction effects during the simulation and enabled extraction of spectral phases associated with the individual spin-orbit-split thresholds [15,17,24]. RABBITT simulations were carried out for several driving IR wavelengths, scanning across the resonance.

We separated the photoelectron spectra coupled to each of the $j = 1/2$ and $j = 3/2$ Ar^+ final states to obtain the energy-resolved spectral phase contributions of each SO

component and compared these to published experimental results [13].

We resolved spectral phase in energy and emission angle, observing variations in the spectral phase as a function of emission angle between energies across the sideband interval, induced by the $3s^{-1}4p$ resonance. By calculating the spectral phase resolved in energy and angle (SPREA) for the $j = 1/2$ and $j = 3/2$ components separately, we confirm that the $j = 1/2$ component SPREA is almost identical to that of the $j = 3/2$ component, shifted by the SO splitting energy of 177 meV. This suggests that for light systems with weak SO interactions, the approximation developed in Ref. [32] for mapping nonrelativistic computational results to a relativistic (SO-split) picture is a valid approach.

In contrast to other available methods, the RMT approach can describe the evolution of SO dynamics [15]. For heavier systems, e.g., krypton, the SO interaction will cause more pronounced dynamics. These dynamics are sufficiently fast to evolve during the laser pulse and thus will certainly play a role in the phase extracted from RABBITT experiments. It will be interesting to assess the impact this has, and whether information about the SO dynamics can be extracted from RABBITT-type experiments.

All data and codes used to obtain the photoelectron spectra presented in this paper are available for reproducibility in Ref. [33], with an additional suite of tools to extract the associated SPREAs available in Ref. [31].

ACKNOWLEDGMENTS

We thank Dr. C. Ballance (Astrophysics Research Centre, Queen's University Belfast) for valuable discussions around the design of the atomic structure. The RMT code is part of the UK-AMOR suite, and can be obtained for free on Gitlab [34]. This work benefited from computational support by CoSeC, the Computational Science Centre for Research Communities, through CCPQ. The authors acknowledge funding from the UK Engineering and Physical Sciences Research Council (EPSRC) under Grants No. EP/P022146/1, No. EP/P013953/1, No. EP/R029342/1, No. EP/T019530/1, and No. EP/V05208X/1. This work relied on the ARCHER2 UK National Supercomputing Service [35], for which access was obtained via the UK-AMOR consortium funded by EP-SRC.

- [1] M. Maiuri, M. Garavelli, and G. Cerullo, Ultrafast spectroscopy: State of the art and open challenges, *J. Am. Chem. Soc.* **142**, 3 (2020).
- [2] G. Roberts, Interference effects in femtosecond spectroscopy, *Philos. Trans. R. Soc. London A* **360**, 987 (2002).
- [3] V. Vénier, R. Taïeb, and A. Maquet, Phase dependence of $(N + 1)$ -color ($N > 1$) IR-UV photoionization of atoms with higher harmonics, *Phys. Rev. A* **54**, 721 (1996).
- [4] H. G. Muller, Reconstruction of attosecond harmonic beating by interference of two-photon transitions, *Appl. Phys. B* **74**, s17 (2002).
- [5] Á. J. Galán, L. Argenti, and F. Martín, Modulation of attosecond beating by resonant two-photon transition, *J. Phys.: Conf. Ser.* **635**, 012005 (2015).
- [6] L. Cattaneo, J. Vos, M. Lucchini, L. Gallmann, C. Cirelli, and U. Keller, Comparison of attosecond streaking and RABBITT, *Opt. Express* **24**, 29060 (2016).
- [7] M. Isinger, D. Busto, S. Mikaelsson, S. Zhong, C. Guo, P. Salières, C. L. Arnold, A. L'Huillier, and M. Gisselbrecht, Accuracy and precision of the RABBITT technique, *Philos. Trans. R. Soc. A* **377**, 20170475 (2019).
- [8] L. Gallmann, I. Jordan, H. J. Wörner, L. Castiglioni, M. Hengsberger, J. Osterwalder, C. A. Arrell, M. Chergui, E.

- Liberatore, U. Rothlisberger, and U. Keller, Photoemission and photoionization time delays and rates, *Struct. Dyn.* **4**, 061502 (2017).
- [9] J. M. Dahlström, A. L'Huillier, and A. Maquet, Introduction to attosecond delays in photoionization, *J. Phys. B: At. Mol. Opt. Phys.* **45**, 183001 (2012).
- [10] P. M. Paul, E. S. Toma, P. Breger, G. Mullot, F. Auge, P. Balcou, H. G. Muller, and P. Agostini, Observation of a train of attosecond pulses from high harmonic generation, *Science* **292**, 1689 (2001).
- [11] V. Gruson, L. Barreau, A. Jimenez-Galan, F. Risoud, J. Caillat, A. Maquet, B. Carre, F. Lepetit, J. F. Hergott, T. Ruchon, L. Argenti, R. Taieb, F. Martin, and P. Salieres, Attosecond dynamics through a fano resonance: Monitoring the birth of a photoelectron, *Science* **354**, 734 (2016).
- [12] D. Busto, L. Barreau, M. Isinger, M. Turconi, C. Alexandridi, A. Harth, Zhong, S., R. J. Squibb, D. Kroon, S. Plogmaker, M. Miranda, Á. Jiménez-Galán, L. Argenti, C. L. Arnold, R. Feifel, F. Martín, M. Gisselbrecht, A. L'Huillier, and P. Salieres, Time-frequency representation of autoionization dynamics in helium, *J. Phys. B: At. Mol. Opt. Phys.* **51**, 044002 (2018).
- [13] M. Turconi, L. Barreau, D. Busto, M. Isinger, C. Alexandridi, A. Harth, R. Squibb, D. Kroon, R. Arnold, C. Feifel, M. Gisselbrecht, L. Argenti, F. Martín, A. L'Huillier, and P. Salieres, Spin-orbit-resolved spectral phase measurements around a fano resonance, *J. Phys. B: At. Mol. Opt. Phys.* **53**, 184003 (2020).
- [14] M. Zürch, H.-T. Chang, L. J. Borja, P. M. Kraus, S. K. Cushing, A. Gandman, C. J. Kaplan, M. Hwan Oh, J. S. Prell, D. Prendergast, C. D. Pemmaraju, D. M. Neumark, and S. R. Leone, Direct and simultaneous observation of ultrafast electron and hole dynamics in germanium, *Nat. Commun.* **8**, 15734 (2017).
- [15] J. Wragg, D. D. A. Clarke, G. S. J. Armstrong, A. C. Brown, C. P. Ballance, and H. W. van der Hart, Resolving Ultrafast Spin-Orbit Dynamics in Heavy Many-Electron Atoms, *Phys. Rev. Lett.* **123**, 163001 (2019).
- [16] A. C. Brown, G. S. J. Armstrong, J. Benda, D. D. A. Clarke, J. Wragg, K. R. Hamilton, Z. Mašín, J. D. Gorfinkiel, and H. W. van der Hart, RMT: R-matrix with time-dependence. solving the semi-relativistic, time-dependent Schrödinger equation for general, multielectron atoms and molecules in intense, ultrashort, arbitrarily polarized laser pulses, *Comput. Phys. Commun.* **250**, 107062 (2020).
- [17] G. S. J. Armstrong, D. D. A. Clarke, J. Benda, J. Wragg, A. C. Brown, and H. W. van der Hart, Enhancing spin polarization using ultrafast angular streaking, *Phys. Rev. A* **103**, 053123 (2021).
- [18] P. Hockett, Angle-resolved RABBITT: Theory and numerics, *J. Phys. B* **50**, 154002 (2017).
- [19] W. Jiang, G. S. J. Armstrong, J. Tong, Y. Xu, Z. Zuo, J. Qiang, P. Lu, D. D. A. Clarke, J. Benda, A. Fleischer, H. Ni, K. Ueda, H. W. van der Hart, A. C. Brown, X. Gong, and J. Wu, Atomic partial wave meter by attosecond coincidence metrology, *Nat. Commun.* **13**, 5072 (2022).
- [20] S. Saha, J. Vinbladh, J. Sörngård, A. Ljungdahl, and E. Lindroth, Angular anisotropy parameters for photoionization delays, *Phys. Rev. A* **104**, 033108 (2021).
- [21] A. Autuori, D. Platzter, M. Lejman, G. Gallician, L. Maëder, A. Covolo, L. Bosse, M. Dalui, D. Bresteau, J.-F. Hergott, O. Tcherbakoff, H. J. B. Marroux, V. Lorient, F. Lépine, L. Poisson, R. Taieb, J. Caillat, and P. Salieres, Anisotropic dynamics of two-photon ionization: An attosecond movie of photoemission, *Sci. Adv.* **8**, eabl7594 (2022).
- [22] A. S. Kheifets and A. W. Bray, RABBITT phase transition across the ionization threshold, *Phys. Rev. A* **103**, L011101 (2021).
- [23] A. Pradhan, S. Nahar, J. Oelgoetz, P. G. Burke, V. M. Burke, A. Sunderland, and C. Noble, R-matrix ii approach to electron correlations in heavy atomic systems, in *APS Division of Atomic, Molecular and Optical Physics Meeting Abstracts*, APS Meeting Abstracts (2004), p. F4.011
- [24] K. A. Berrington, W. B. Eissner, and P. H. Norrington, Rmatrix1: Belfast atomic R-matrix codes, *Comput. Phys. Commun.* **92**, 290 (1995).
- [25] P. G. Burke and K. T. Taylor, R-matrix theory of photoionization. Application to neon and argon, *J. Phys. B* **8**, 2620 (1975).
- [26] K. Bartschat, E. T. Hudson, M. P. Scott, P. G. Burke, and V. M. Burke, Electron-atom scattering at low and intermediate energies using a pseudo-state/R-matrix basis, *J. Phys. B: At., Mol. Opt. Phys.* **29**, 115 (1996).
- [27] A. Kramida, Y. Ralchenko, J. Reader, and N. A. Team, NIST atomic spectra database (ver. 5.9) (2021).
- [28] M. A. Branch, T. F. Coleman, and Y. Li, A subspace, interior, and conjugate gradient method for large-scale bound-constrained minimization problems, *SIAM J. Sci. Comput.* **21**, 1 (1999).
- [29] S. Donsa, M. Ederer, R. Pazourek, J. Burgdörfer, and I. Březinová, Angle-resolved time delays for shake-up ionization of helium, *Phys. Rev. A* **102**, 033112 (2020).
- [30] A. S. Kheifets, Strongly resonant reconstruction of attosecond beating by interference of two-photon transitions on lithium, *Phys. Rev. A* **104**, L021103 (2021).
- [31] L. F. Roantree, Data and code for "Energy- and angle resolved spectral phases via semi-relativistic ab-initio RABBITT simulations", https://gitlab.com/lukeroantree/argon_rabbitt_scripts/-/releases/v1.0.0 (2022).
- [32] M. Kotur *et al.*, Spectral phase measurement of a fano resonance using tunable attosecond pulses, *Nat. Commun.* **7**, 10566 (2016).
- [33] L. F. Roantree, Triple-resolution of spectral phases via semi-relativistic ab-initio RABBITT simulations DATA & WORKFLOW (v1.0.0) [Data set], Zenodo (2022), <https://doi.org/10.5281/zenodo.7148018>.
- [34] A. C. Brown *et al.*, The RMT code, <https://gitlab.com/Uk-amor/RMT> (2023).
- [35] Edinburgh Parallel Computing Centre, The ARCHER2 UK National Supercomputing Service (2021), <https://www.archer2.ac.uk>.